Progress in optical Thomson scattering diagnostics for ICF gas-filled hohlraums

View Online   Export Citation   CrossMark

Hang Zhao,[1,2] Zhichao Li,[1,a)] Dong Yang,[1] Xin Li,[3] Yaohua Chen,[3] Xiaohua Jiang,[1] Yonggang Liu,[1] Tao Gong,[1] Liang Guo,[1] Sanwei Li,[1] Qi Li,[1] Feng Wang,[1] Shenye Liu,[1] Jiamin Yang,[1] Shaoen Jiang,[1] Wanguo Zheng,[1] Baohan Zhang,[1] and Yongkun Ding[3,a)]

AFFILIATIONS

[1] Laser Fusion Research Center, China Academy of Engineering Physics, Mianyang 621900, China
[2] Tsinghua University, Beijing 100084, China
[3] Institute of Applied Physics and Computational Mathematics, Beijing 100088, China

[a)]Authors to whom correspondence should be addressed: lizhi@mail.ustc.edu.cn and ding-yk@vip.sina.com

ABSTRACT

Optical Thomson scattering (OTS) diagnostics have been continuously developed on a series of large laser facilities for inertial confinement fusion (ICF) research in China. We review recent progress in the use of OTS diagnostics to study the internal plasma conditions of ICF gas-filled hohlraums. We establish the predictive capability for experiments by calculating the time-resolved Thomson scattering spectra based on the 2D radiation-hydrodynamic code LARED, and we explore the fitting method for the measured spectra. A typical experiment with a simplified cylindrical hohlraum is conducted on a 10 kJ-level laser facility, and the plasma evolution around the laser entrance hole is analyzed. The dynamic effects of the blast wave from the covering membrane and the convergence of shocks on the hohlraum axis are observed, and the experimental results agree well with those of simulations. Another typical experiment with an octahedral spherical hohlraum is conducted on a 100 kJ-level laser facility, and the plasma evolution at the hohlraum center is analyzed. A discrepancy appears between experiment and simulation as the electron temperature rises, indicating the occurrence of nonlocal thermal conduction.

I. INTRODUCTION

In indirect-drive inertial confinement fusion (ICF),[1] hohlraum targets made of high-Z material are employed to convert the incident laser energy to X rays to drive the implosion, and, for symmetry control, the hohlraum is commonly filled with a low-Z gas to suppress the expansion of the high-Z plasma from the hohlraum wall. Therefore, for an ignition hohlraum, the internal plasma conditions are quite complex, with plasmas generated from the hohlraum wall, the infill gas, and the ablator of the fuel pellet interacting with each other. Owing to these complex and unexpected internal plasma conditions, problems connected with laser plasma interaction (LPI)[2] are among the most serious that arise in attempts to achieve ignition, and they remain unsolved in the National Ignition Campaign (NIC)[3] conducted on the National Ignition Facility (NIF),[4] the largest ICF laser facility in the world at present. To improve hohlraum performance, it is essential to gain a better understanding of laser–hohlraum energy coupling and the relevant physics concerning LPI, energy

deposition, and X-ray conversion. To achieve this, the internal plasma conditions need to be precisely diagnosed experimentally, and the dynamic and kinetic effects relevant to hohlraum plasma evolution need to be thoroughly investigated. However, measurement of hohlraum plasma conditions is quite challenging, owing to the complex experimental environment on large laser facilities and the closed geometry of hohlraum targets. Therefore, it is critical to develop an appropriate diagnostic for hohlraum plasma conditions.

Among the various plasma diagnostic methods that are available, optical Thomson scattering (OTS)[5] is one of the best choices, since it is capable of providing unperturbed, local, and precise measurements.[6,7] OTS diagnostic measures the scattering spectra of an incident laser by free electrons within a plasma, which directly reflect electron motion and are sensitive to intrinsic plasma density fluctuations. With an appropriate experimental design, OTS can diagnose a variety of plasma parameters,[6–9] including the electron temperature, the electron density, the plasma flow velocity, the ion temperature, the averaged ionization state, and the ion species

fraction. Hence, applying OTS to ICF hohlraums will greatly enhance diagnostic capacity and help to understand hohlraum plasma behavior. However, despite the advantages of OTS in plasma characterization, its experimental implementation is still challenging. The primary reason is that the Thomson scattering cross section is quite small—under typical conditions, the intensity of the scattered light is nine orders of magnitude weaker than that of the incident light. Therefore, a high-energy probe beam is often required, and the experimental setup needs to be very carefully designed to avoid strong background noise and obtain an acceptable signal-to-noise ratio.

Throughout the development of the OTS diagnostic for ICF purposes, research groups in the United States have made a remarkable contribution. The first Thomson scattering experiment for ICF hohlraum targets was conducted on the NOVA laser facility[10] with a 2ω (526.6 nm) probe laser, and the electron temperature, ion temperature, and plasma flow velocity in the gas-filled region were measured. Subsequently, the OTS diagnostic was upgraded, with the use of a 4ω (263.3 nm) probe laser.[11] For this wavelength band, there is less light absorption in the plasma, and the critical density is higher, which allows measurements to be made in higher-density regions. In addition, the background noise of stimulated Raman side scattering from the 3ω (351 nm) drive beams can be avoided. Since then, 4ω probe lasers have been commonly used for ICF hohlraums, and OTS has been continuously developed on the OMEGA laser facility,[12] where multicolor Thomson scattering[13] and imaging Thomson scattering[14] were implemented. To further reduce background noise from 3ω drive beams in an ignition-scale hohlraum, a 5ω (210 nm) OTS diagnostic has also been designed on the NIF,[15] which is quite challenging for deep-ultraviolet optical transmission and detection.

In China, we have also developed OTS diagnostics for ICF research. Early experiments were conducted on the Xingguang-II laser facility[16] with a 2ω probe beam and on the Shenguang-II laser facility[17,18] with a 4ω probe beam. They focused mainly on targets with open geometry, such as disk targets and gas-bag targets, which provide simpler plasma conditions than hohlraums. These early explorations have played an important role in understanding the behavior of laser-produced plasmas and have paved the way for OTS experiments with hohlraum targets. In recent years, 4ω OTS diagnostics have been successively implemented on 10 kJ-level[19] and 100 kJ-level[20] laser facilities, and our research focus has been on the internal plasma conditions of gas-filled hohlraums. To reduce the complexity of hohlraum plasma conditions in the preliminary study, we have adopted hohlraums without any pellets inside. To establish the predictive capability of our experiments, we have developed a method to simulate time-resolved Thomson scattering spectra, where the input plasma conditions are given by the 2D radiation-hydrodynamic code LARED.[21] The simulated spectra can provide guidance for experimental measurements and can be compared directly with the measured spectra. To analyze the accuracy of measurement of plasma parameters, we have also explored the fitting method for Thomson scattering spectra. Recent experiments have involved different types of hohlraums. A typical experiment with a simplified cylindrical hohlraum has been conducted on the 10 kJ-level laser facility, where the geometry was kept quasi-2D to facilitate comparisons with simulations. The plasma evolution around the laser entrance hole (LEH) has been studied, and the experimental results are in good agreement with the simulations. The dynamic effects of

the blast wave generated from the covering membrane and the convergence of shocks on the hohlraum axis have been observed. Another experiment with an octahedral spherical hohlraum[22] has been conducted on the 100 kJ-level laser facility, and the plasma evolution at the center of the hohlraum has been studied. A major discrepancy appears between experiment and simulation as the electron temperature rises, indicating the occurrence of nonlocal thermal conduction, which has not been considered in the simulation code.

In this paper, we briefly review progress in recent explorations of the measurement of internal plasma conditions in gas-filled hohlraums. In Sec. II, we present the model for the Thomson scattering spectra calculation, including spectral fitting of experimental data and spectral simulation based on LARED, which are two helpful ways to understand the behavior of hohlraum plasmas. In Sec. III, we describe the experiment on the simplified cylindrical hohlraum, and discuss the plasma evolution in the LEH region. In Sec. IV, we describe the experiment on the octahedral spherical hohlraum, and discuss the plasma conditions at the hohlraum center. Section V is a summary.

II. MODEL FOR THOMSON SCATTERING SPECTRA CALCULATION

A. Theoretical basis

For a probe laser with intensity I_0, frequency ω_i, and wave vector $\boldsymbol{k}_i$, the power of Thomson-scattered light with wave vector $\boldsymbol{k}_s$ in solid angle $d\Omega$ and in the frequency range from ω_s to $\omega_s + d\omega$ is[5]

$$P_s d\Omega d\omega = \frac{1}{2\pi} I_0 r_e^2 V n_e \left(1 + \frac{2\omega}{\omega_i}\right) \sin^2 \varphi S(\boldsymbol{k}, \omega) d\Omega d\omega, \quad (1)$$

where $\omega = \omega_s - \omega_i$ and $\boldsymbol{k} = \boldsymbol{k}_s - \boldsymbol{k}_i$ are the frequency and wave vector of the probed mode of plasma density fluctuations, r_e is the classical electron radius, V is the scattering volume, n_e is the electron number density, φ is the angle between the polarization direction of the incident light and the propagation direction of the scattered light, and $S(\boldsymbol{k}, \omega)$ is the spectral density function.

The spectral density function $S(\boldsymbol{k}, \omega)$ for plasmas with multiple ion species can be expressed as[5]

$$S(\boldsymbol{k}, \omega) = \frac{2\pi}{k} \left|1 - \frac{\chi_e}{\epsilon}\right|^2 f_{e0}\left(\frac{\omega}{k}\right) + \frac{2\pi}{k} \left|\frac{\chi_e}{\epsilon}\right|^2 \sum_j \frac{Z_j^2 N_j}{\sum_j Z_j N_j} f_{i0,j}\left(\frac{\omega}{k}\right), \quad (2)$$

where the subscript j stands for the jth ion species, Z_j is the ion charge, N_j is the ion number density, χ_e (χ_j) and f_{e0} ($f_{i0,j}$) are the electron (ion) susceptibility and the normalized 1D electron (ion) velocity distribution function, respectively, and $\epsilon = 1 + \chi_e + \sum_j \chi_j$ is the plasma dielectric function.

The scattering parameter is defined as $\alpha \equiv 1/k\lambda_{De}$, where λ_{De} is the Debye length. When $\alpha > 1$, collective scattering from intrinsic plasma wave modes dominates, and resonant features related to ion-acoustic waves (IAWs) and electron plasma waves (EPWs) can be observed in the scattered spectra. For measurement at a specific scattering angle, the plasma waves co- and counter-propagating along $\boldsymbol{k}$ are probed, and the frequency differences between the scattered and the incident light in the laboratory frame are determined by the frequencies of plasma waves and the Doppler shift caused by plasma flow,[7] which are

$$\Delta\omega_{\pm \text{IAW}} = \pm\omega_{\text{IAW}} + (\boldsymbol{k}_s - \boldsymbol{k}_i) \cdot \boldsymbol{u} = \pm k c_s + \boldsymbol{k} \cdot \boldsymbol{u} \quad (3)$$

for the IAW features and

$$\Delta\omega_{\pm \text{EPW}} = \pm\omega_{\text{EPW}} + (\boldsymbol{k}_s - \boldsymbol{k}_i) \cdot \boldsymbol{u} = \pm\sqrt{\omega_{pe}^2 + 3k^2 v_{te}^2} + \boldsymbol{k} \cdot \boldsymbol{u} \quad (4)$$

for the EPW features, where $\Delta\omega_{\pm}$ correspond to the blue- and red-shifted resonant features, $\boldsymbol{u}$ is the plasma flow velocity, $c_s \cong \sqrt{(ZT_e + 3T_i)/m_i}$ is the ion sound speed (T_e and T_i are the electron and ion temperatures, and m_i is the ion mass), ω_{pe} is the plasma frequency, and v_{te} is the root-mean-square (rms) thermal speed of electrons. Equations (3) and (4) show that the IAW features are sensitive to ZT_e, T_i, and $\boldsymbol{u}$, while the EPW features are mainly sensitive to n_e, since the dominant term in Eq. (4) is $\omega_{pe}^2 \propto n_e$. In practice, the plasma parameters are obtained by fitting the spectra calculated with Eqs. (1) and (2) to those measured by experiment.

B. Spectral fitting

In spectral fitting for high-temperature (>1 keV) hohlraum plasmas, the Thomson scattering theory of collisionless, unmagnetized plasmas with Maxwellian distributions is most commonly used. For Maxwellian distributions, the functions f_{e0} and $f_{i0,j}$ in Eq. (2) take the forms

$$f_{e0}(v) = \frac{1}{\sqrt{2\pi}v_{te}}\exp\left(-\frac{v^2}{2v_{te}^2}\right), \quad (5)$$

$$f_{i0,j}(v) = \frac{1}{\sqrt{2\pi}v_{tj}}\exp\left(-\frac{v^2}{2v_{tj}^2}\right), \quad (6)$$

where v_{te} and v_{tj} are the rms thermal speeds of electrons and the jth species of ions, respectively, and the electron and ion susceptibilities χ_e and χ_j in Eq. (2) take the forms

$$\chi_e(\boldsymbol{k},\omega) = \alpha^2 w(x_e), \quad (7)$$

$$\chi_j(\boldsymbol{k},\omega) = \alpha^2 \frac{Z_j^2 N_j}{\sum_j Z_j N_j} \frac{T_e}{T_j} w(x_j), \quad (8)$$

where $x_e = \omega/(\sqrt{2}\,kv_{te})$, $x_j = \omega/(\sqrt{2}\,kv_{tj})$, and

$$w(x) = 1 - 2xe^{-x^2}\int_0^x e^{p^2}\,dp + i\sqrt{\pi}xe^{-x^2}. \quad (9)$$

When dealing with collisional effects[23] or non-Maxwellian distributions,[24] the expressions above for susceptibilities and distribution functions should be modified.

Least-squares fitting is performed to infer the plasma parameters from the experimental data. The problem can be described as finding the input X that minimizes the quantity

$$r \equiv \sum_\lambda \left[P_{fit}(\lambda, X) - P_{exp}(\lambda)\right]^2,$$

where X represents the parameters to be inferred, λ is the measured wavelength corresponding to the camera pixels, and P_{fit} and P_{exp} are the calculated and measured Thomson scattering power spectra, respectively. Generally, the input X for the IAW features contains the electron temperature T_e, the ion temperature T_i, the plasma flow velocity $\boldsymbol{u}$, and the electron drift velocity $\boldsymbol{u}_d$, where $\boldsymbol{u}$ contributes to the Doppler shift, while $\boldsymbol{u}_d$ contributes to the difference in Landau damping and thus the asymmetry of the blueshifted and redshifted

features. These velocities are included in the calculation by substituting $\omega = \omega_s - \omega_i - \boldsymbol{k} \cdot \boldsymbol{u}$ into f_{i0} and χ_i, while substituting $\omega = \omega_s - \omega_i - \boldsymbol{k} \cdot (\boldsymbol{u} + \boldsymbol{u}_d)$ into f_{e0} and χ_e in Eqs. (5)–(9). Other parameters required in the calculation, such as the electron density and the ion charge, are assumed in the fitting for the IAW features.

When calculating P_{fit}, the instrumental effects (spectral response and resolution) and the background noise in the experiment should be taken into account. For the IAW features, the background can be approximated as linear in spectrum, and P_{fit} can be written as

$$P_{fit}(\lambda, X) = AP_{signal}(\lambda, T_e, T_i, u_{ik}, u_{ek}) + B_1 + \frac{B_2 - B_1}{\lambda_2 - \lambda_1}(\lambda - \lambda_1),$$

$$(10)$$

where P_{signal} is normalized by its maximum, A is the relative amplitude of the signal, B_1 and B_2 are the relative background levels at the two sampled ends λ_1 and λ_2, respectively, $u_{ik} \equiv \boldsymbol{k} \cdot \boldsymbol{u}$, and $u_{ek} \equiv \boldsymbol{k} \cdot (\boldsymbol{u} + \boldsymbol{u}_d)$. Hence, X involves seven variables (T_e, T_i, u_{ik}, u_{ek}, A, B_1, B_2) to be fitted. Figures 1(a)–1(c) show three examples of the spectral fitting, with different temperature levels. The samples in Figs. 1(a) and 1(b) are extracted from the data from the octahedral spherical hohlraum experiment [see Sec. IV, Fig. 10(a); the samples are taken at 2 ns and 4.3 ns, respectively], while the sample in Fig. 1(c) is extracted from the data from the cylindrical hohlraum experiment [see Sec. III, Fig. 5(a); the sample is taken at 2.2 ns].

To evaluate the uncertainty of the fitting process, we can consider the quantity

$$R \equiv \frac{1}{A_{fit}}\sqrt{\frac{r}{N}},$$

where r is the sum of squares defined above, N is the total number of terms in the summation, and A_{fit} is the best-fit signal amplitude corresponding to the A in Eq. (10). By definition, R reaches a minimum at the best-fit point, and R_{min} characterizes the noise-to-signal ratio in the fitting process. Figures 1(d)–1(f) show the contours of the difference $\Delta R = R - R_{\text{min}}$ around the best-fit point in the T_e–T_i plane, corresponding to Figs. 1(a)–1(c), respectively. These contours reflect the parameter sensitivities and can be used to estimate the fitting uncertainty. For instance, taking the contours of 0.005 in Figs. 1(d)–1(f), the relative uncertainties for electron (ion) temperature are estimated to be ±9% (±30%), ±10% (±24%), and ±9% (±10%), respectively.

As a comparison, the best-fit points of different spectrum samples within ±100 ps are shown in these contour maps. In practice, each sample is extracted from a one-pixel time interval of the original spectral image. The fluctuation of the best-fit points can also be used to estimate the fitting uncertainty, since the plasma parameters vary slightly within ±100 ps. Taking the standard deviation of these points in Figs. 1(d)–1(f), the relative uncertainties for electron (ion) temperature are estimated to be ±9% (±22%), ±3% (±15%), and ±5% (±10%), respectively, which are within the uncertainties estimated by the contours mentioned above.

For further evaluation, the effects of plasma gradients and k-vector smearing should be considered. However, for the discussion in this paper, the k-vector smearing effect is quite small, since the scattered light is collected in an $f/10$ cone and the k variance is only about ±2.5%. The fitting results considering these two effects are also
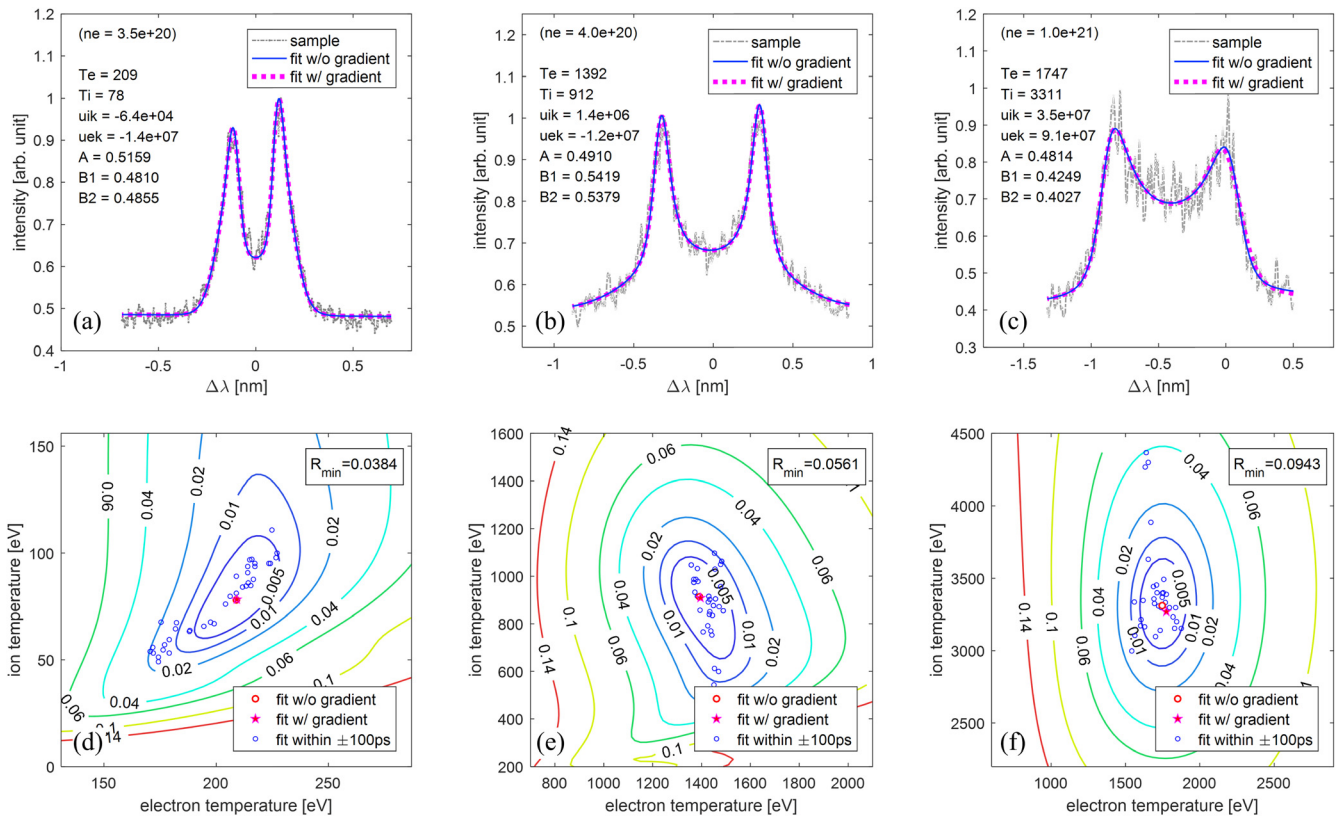
FIG. 1. Examples of Thomson scattering spectral fitting. (a), (b), and (c) are three cases with different temperature levels and signal-to-noise ratios. These samples are the IAW features of 4ω Thomson scattering from pentane (C_5H_{12}) plasmas. The horizontal axes are labeled with the wavelength shift relative to 263.3 nm. The blue solid lines and the magenta dashed lines are the best-fit spectra without and with consideration of plasma gradients and k-vector smearing, respectively. The seven quantities listed on the left are the best fits without gradient (T_e and T_i are in units of eV; u_{ik} and u_{ek} are in cm/s; A, B_1, and B_2 are dimensionless). The electron density (n_e in cm^{-3}) is assumed according to simulation. (d)–(f) show the contours of $\Delta R = R - R_{min}$ (the definition of R is given in Sec. II B) around best-fit points in the T_e–T_i plane, corresponding to (a), (b), and (c), respectively. The points of R_{min} are marked by red circles, and the best-fit points with gradient are marked by stars. The best-fit points of different samples within ± 100 ps are marked by blue circles. The distribution of these points indicates that the contour of 0.005 can be taken as an appropriate estimate of the fitting uncertainty.

shown in Figs. 1(d)–1(f). The plasma gradients in the fitting process are given by radiation-hydrodynamic simulations. In Figs. 1(d) and 1(e), the gradients are small, with a T_e variation of $\pm 5\%$ and a T_i variation of $\pm 10\%$, and thus the best-fit points almost coincide with those obtained without considering gradients. In Fig. 1(f), the gradients are larger, with a T_e variation of $\pm 5\%$, a T_i variation of $\pm 20\%$, and a u_{ik} variation of $\pm 12\%$. As a result, the best-fit point shifts a little, but is still close to the point without gradient.

In addition, the pre-assumption of electron density also has an influence on the fitting result. Figure 2 shows the variation of the best-fit temperatures when assuming different electron densities in the fitting process. The corresponding spectrum is the one shown in Fig. 1(b). According to simulation, the electron density within the Thomson scattering volume varies from 3×10^{20} to 5×10^{20} cm^{-3}, as shown in the shaded area of Fig. 2. Therefore, the uncertainties in the electron (ion) temperature induced by the density assumption are estimated to be $\pm 6\%$ ($\pm 1\%$). For a general consideration, a Monte Carlo approach can be applied in error analysis.[7]

C. Spectral simulation

The aim of Thomson scattering spectral simulation is to build up the predictive capability for experiments, which contributes to experimental design and data analysis. The spectra are calculated according to Eqs. (1)–(9), using the plasma conditions given by the 2D radiation-hydrodynamic code LARED.[21]

Figure 3(a) shows an example of simulation with cylindrical symmetry, where the Z direction is along the hohlraum axis and the R direction is along the hohlraum radius. The Thomson scattering volume is defined by the overlap of the probe beam and the diagnostic aperture, as shown in Fig. 3(b), where the whole scattering volume is divided into a number of volume elements for consideration of plasma inhomogeneity. Each element is assigned a 2D coordinate (Z, R) and a set of plasma parameters (T_e, T_i, n_e, etc.) corresponding to the positions in the simulation, and the Thomson scattering spectra at each volume element are calculated separately and then summed. The solid angle $d\Omega$ in Eq. (1) is determined by the f-number F of the collecting optics. For the $f/10$ collection system used in our experiments, the solid angle is quite small and can be approximated as
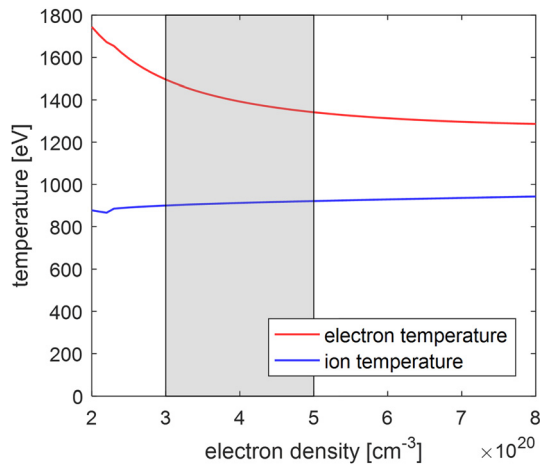
FIG. 2. Influence of the n_e assumption on temperature (T_e, T_i) fitting results. The curves show the best-fit temperatures at given electron densities. The corresponding spectrum is shown in Fig. 1(b). The shaded area shows the density range given by radiation-hydrodynamic simulation.

$d\Omega \cong \pi/(4F^2)$. The spectral response, the spectral resolution, and the inverse bremsstrahlung absorption[25] along the optical path are also involved in the calculation. Finally, the spectra calculated at different time are synthesized as time-resolved spectra, with temporal resolution accounted for.

III. THOMSON SCATTERING EXPERIMENT WITH SIMPLIFIED CYLINDRICAL HOHLRAUM

In this section, we review a typical experiment with a simplified cylindrical hohlraum, as shown in Fig. 4. The target is a cylindrical gold hohlraum with two open ends as LEHs, and both the diameter and the length of the hohlraum are 1.4 mm. The hohlraum is filled
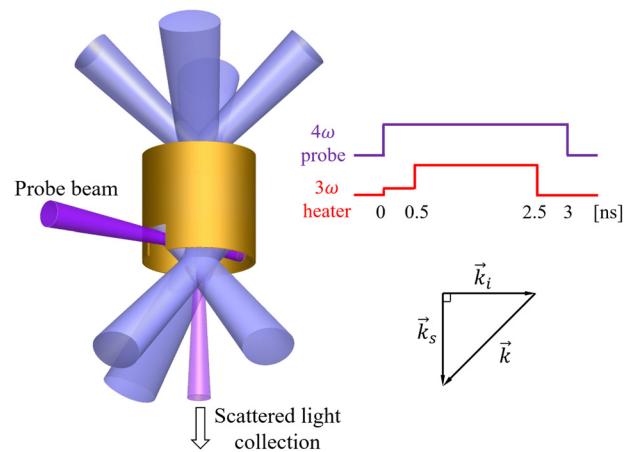

FIG. 4. Thomson scattering setup for a simplified cylindrical hohlraum. The hohlraum is filled with 0.6 atm C_5H_{12} (the covering membrane for gas filling is not shown) and is heated by seven heater beams, with a total energy of ~5.6 kJ, and the heater pulse consists of a 2 ns main pulse and a 0.5 ns pre-pulse. The probe beam is aligned horizontally and enters the hohlraum through the diagnostic hole, with 90 J energy in a 3 ns pulse, which is synchronized to the pre-pulse of the heater beams. The scattered light is collected downward, with a scattering angle of 90°.

with pentane (C_5H_{12}) gas at a pressure of 0.6 atm, corresponding to an electron density of 6×10^{20} cm^{-3} when fully ionized. Seven 3ω (351 nm) heater beams penetrate the hohlraum through both ends, with an angle of 45° relative to the hohlraum axis, delivering a total energy of 5.6 kJ in 2 ns main pulse plus a 0.5 ns pre-pulse. The heater beams are smoothed by continuous phase plates (CPPs), with 500 μm-diameter focal spots in the LEH plane. To retain a quasi-2D geometry, the laser spots on the hohlraum wall are arranged in a single ring in the equatorial plane. The 4ω (263.3 nm) probe beam is aligned horizontally and enters the hohlraum through a diagnostic hole
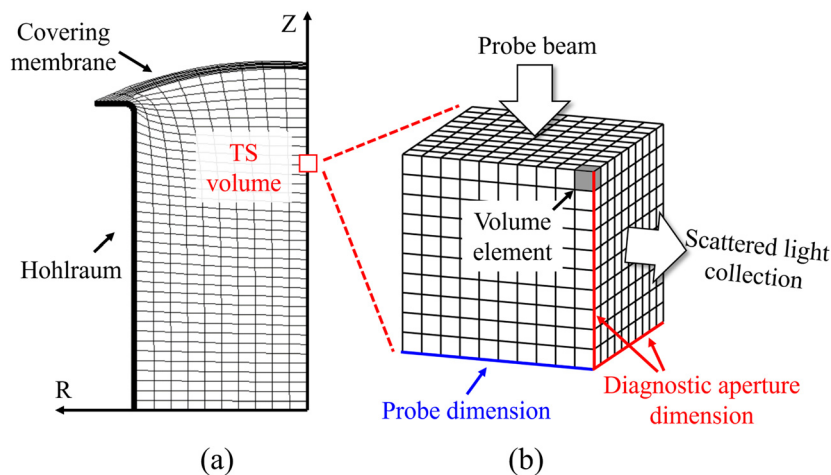

FIG. 3. Schematic diagram of simulation-based calculation of Thomson scattering spectra. (a) An example of hohlraum simulation (the initial grids) with the 2D radiation-hydrodynamic code LARED, which adopts Lagrangian coordinates in the calculation. The Thomson scattering volume is marked on the hohlraum axis. (b) The Thomson scattering volume is divided into a number of volume elements for the consideration of plasma inhomogeneity in spectra calculation.

$(0.35 \times 0.35 \text{ mm}^2)$ on its wall, with 90 J energy in a 3 ns pulse and a $100 \ \mu\text{m}$-diameter focal spot. The probe pulse is synchronized to the heater pre-pulse, and thus is 0.5 ns ahead of the heater main pulse. The scattered light is collected downward, with a scattering angle of 90°, and the scattering volume is $\sim 100 \times 100 \times 100 \ \mu\text{m}^3$, defined by the probe beam and the diagnostic system. A 750 mm-spectrometer and a streak camera are used to record the IAW features of the scattered light, with a spectral resolution of 0.065 nm in full width at half maximum (FWHM).

Figures 5(a) and 5(c) show the measured Thomson scattering spectra from the positions 225 μm inside and 250 μm outside the LEH, respectively, and Figs. 5(b) and 5(d) show the simulated spectra corresponding to Figs. 5(a) and 5(c), respectively. As a rough comparison, the evolution of the IAW features measured by experiment is in accordance with simulation, except for background noise and some differences in detail. In Fig. 5(a), strong noise occurs at the beginning of the heater main pulse ($t = 0.5$ ns), with a bright speck near $\Delta\lambda = 0$ and a broadband stripe, which are probably related to stray light and the LEH covering membrane. In addition, the absence of signal before $t = 0.5$ ns is mainly caused by the covering membrane, which forms a plasma that is too dense to allow transmission of the incident and scattered light at an early stage. In Fig. 5(c), the absence of a signal before 0.4 ns is due to the absence of plasma before the ablated plasma expands into the Thomson scattering region.

Figure 6 shows the evolution of the electron and ion temperatures and the component of the plasma flow velocity along the $\boldsymbol{k}$ direction, corresponding to the two positions measured in the experiment. The triangles and squares with error bars are inferred from the spectra shown in Figs. 5(a) and 5(c), respectively, by the fitting method presented in Sec. II B. The lines are extracted from the radiation-hydrodynamic simulation, and the shaded areas characterize the plasma inhomogeneity within the Thomson scattering volume, as introduced in Sec. II C. As with the comparison in Fig. 5, there is also good agreement between experiment and simulation in Fig. 6.

For the position inside the LEH, the signal continues to weaken from $t = 1$ ns to $t = 2$ ns, as can be seen from Figs. 5(a) and 5(b). This is due to a shock wave (blast wave) from the LEH membrane, generated at the onset of the heater main pulse. Figure 7(a) shows simulation maps of the ion temperature and the electron density at $t = 1$ ns, where the two diagnosed positions are starred in red ($Z = -475$ and $Z = -950$). A shock structure propagating inward can be seen, and the shock front just reaches the position $Z = -475$ at this time. After the shock, a rarefaction wave follows, and the electron density continues to decrease at this position, thus accounting for the decrease in signal intensity. For the measured spectra, the signals from 1.5 ns to 2 ns are so weak that the redshifted features cannot even be recorded.

For both positions, the IAW features show a sharp twist at a late stage (see Fig. 5), which indicates a rapid change in plasma flow
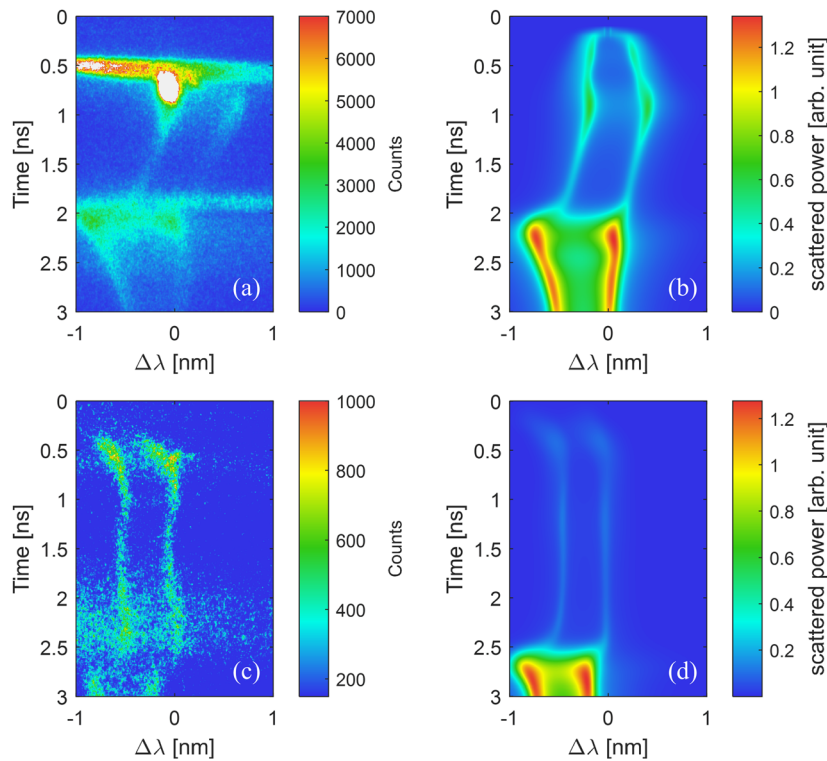

FIG. 5. Comparison of Thomson scattering spectra for the simplified cylindrical hohlraum experiment. (a) and (c) are the experimental data; (b) and (d) are the results of calculations based on radiation-hydrodynamic simulation. (a) and (b) correspond to the position 225 μm inside the bottom LEH, while (c) and (d) correspond to the position 250 μm outside the bottom LEH (see Fig. 4). Both positions are on the hohlraum axis.
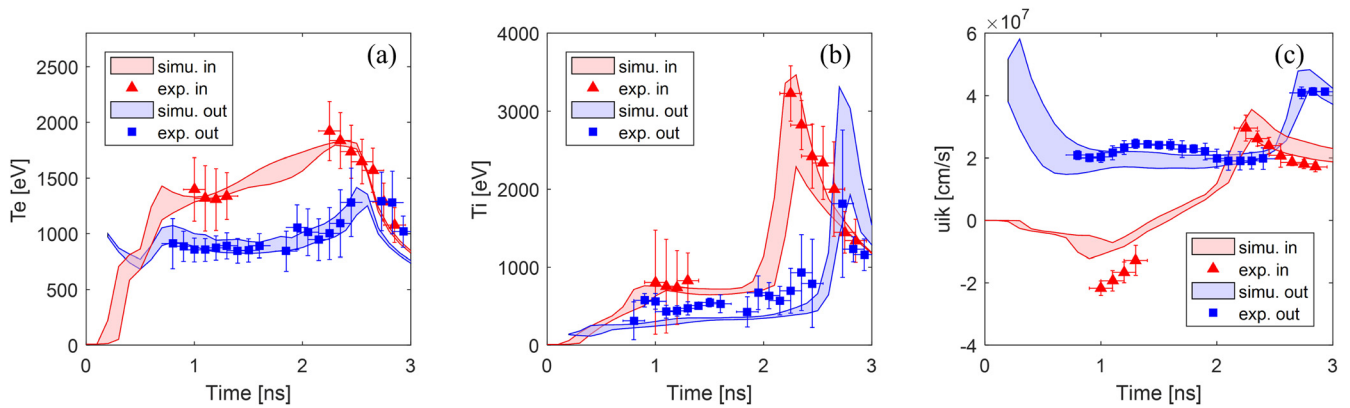
FIG. 6. Evolution of plasma parameters 225 μm inside (red) and 250 μm outside (blue) the LEH. (a) Electron temperature T_e. (b) Ion temperature T_i. (c) Plasma flow velocity $\boldsymbol{u}$ along the $\boldsymbol{k}$ direction. The triangles (inside LEH) and the squares (outside LEH) are inferred from experimental data; the lines are given by the radiation-hydrodynamic simulation, and the shaded areas characterize the plasma inhomogeneity within the Thomson scattering volume.
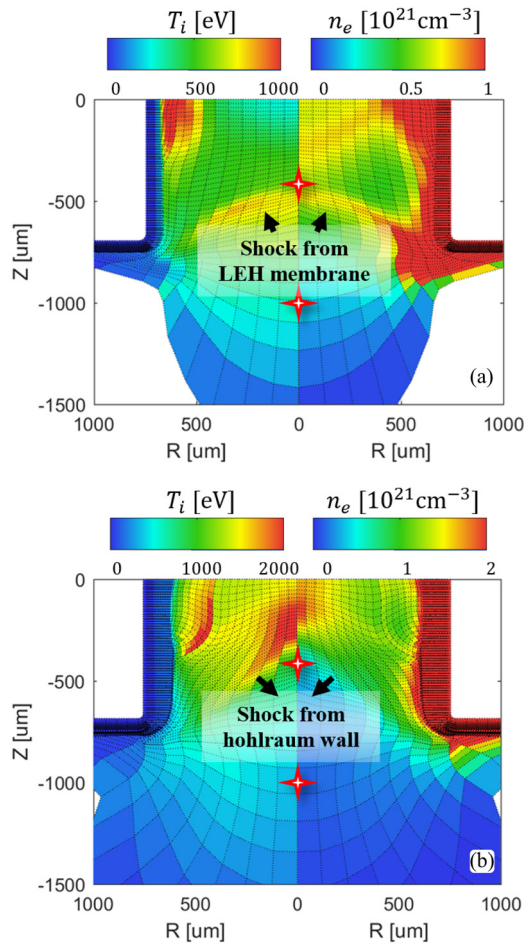

FIG. 7. Cylindrical hohlraum simulation maps for the ion temperature T_i and electron density n_e. The lower half of the hohlraum is shown. (a) is taken at $t = 1$ ns and (b) at $t = 2$ ns. The two diagnosed positions are starred in red: $Z = -475$ and $Z = -950$.

velocity. This change in velocity can be seen in Fig. 6(c), and is also associated with a sharp increase in ion temperature, as shown in Fig. 6(b). This behavior is due to the convergence of shock waves on the hohlraum axis. Figure 7(b) shows simulation maps of the ion temperature and electron density at $t = 2$ ns. A region of high T_i and high n_e forms along the hohlraum axis as the shock waves from the hohlraum wall gradually converge and squeeze the plasma out. This also accounts for the order of time for the change to occur at these two positions: for $Z = -475$, the change occurs at ~2 ns, and for $Z = -950$, the change occurs at ~2.7 ns.

From a more detailed comparison, it is found that there are two main differences between experiment and simulation. First, the signal intensity at a late stage given by simulation is much higher than that actually measured (see Fig. 5), which indicates that convergence of shocks leads to a higher electron density in simulation than experiment. Second, the measured flow velocity inside the LEH [see Fig. 6(c), where the negative velocity is along the $-\boldsymbol{k}$ direction] is larger than in the simulation at an early stage, thus causing a larger redshift in the spectra [see Figs. 5(a) and 5(b)]. These differences are probably caused by the asymmetries in the experiment, especially when there are only three beams heating the hohlraum from the bottom (see Fig. 4). Such asymmetries can weaken the effect of shock convergence, thus reducing the increase in electron density on the hohlraum axis. In addition, the asymmetry of the heater arrangement can also lead to a radial velocity with a component along the $-\boldsymbol{k}$ direction, which accounts for the larger redshift in Fig. 5(a).

IV. THOMSON SCATTERING EXPERIMENT WITH AN OCTAHEDRAL SPHERICAL HOHLRAUM

An octahedral spherical hohlraum[26] is a recently conceived type of hohlraum with a better symmetry than the traditional cylindrical hohlraum and therefore promising for use in ICF ignition. The experimental capabilities of octahedral spherical hohlraums have been developed, and studies of hohlraum energetics have been carried out.[27] After implementation of the OTS diagnostic,[20] we conducted a Thomson scattering experiment to study the internal plasma conditions of a gas-filled octahedral spherical hohlraum. In this section,
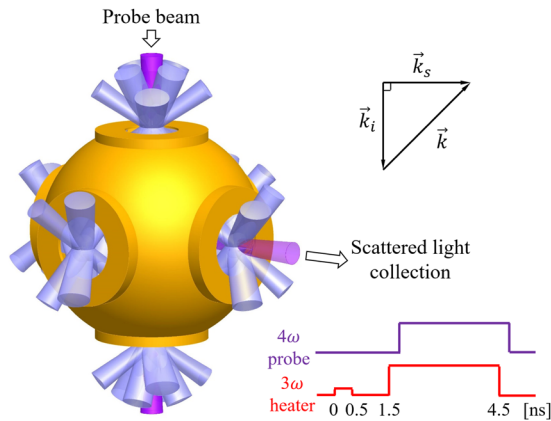
FIG. 8. Thomson scattering setup for an octahedral spherical hohlraum. The hohlraum is heated by 32 heater beams (3ω), with a total energy of 80 kJ (0.5 ns pre-pulse plus 3 ns main pulse, separated by 1 ns). The probe beam (4ω) is aligned vertically and enters the hohlraum through the top LEH, with 90 J energy in a 3 ns pulse, which is delayed by 0.3 ns relative to the heater main pulse. The scattered light is collected horizontally through an equatorial LEH, with a scattering angle of 90°.

we describe the experiment and discuss the results of measurements at the center of the hohlraum.

Figure 8 shows the configuration of the Thomson scattering experiment with an octahedral spherical gold hohlraum (with six LEHs). The hohlraum is filled with pentane (C_5H_{12}) gas at a pressure of 0.35 atm, corresponding to an electron density of $\sim 3.5 \times 10^{20}$ cm^{-3} when fully ionized. The diameters of the hohlraum, the two polar LEHs, and the four equatorial LEHs are 4.8 mm, 1.2 mm and 1.4 mm, respectively. The laser arrangement here is similar to that in the hohlraum energetics experiment,[27] with 32 beams (3ω) heating the hohlraum through six LEHs, delivering a total energy of $\sim$80 kJ. The heater pulse is made up of a 0.5 ns pre-pulse and a 3 ns main pulse, with a 1 ns interval. The 4ω probe beam is aligned vertically and enters

the hohlraum through the top LEH, with 90 J energy in a 3 ns pulse. To reduce the influence of the probe beam on the plasma states, the probe pulse is delayed by 0.3 ns relative to the heater main pulse. The scattered light is collected through an equatorial LEH, with a scattering angle of 90° and a scattering volume of $\sim 100 \times 100 \times 100$ μm^3. Time-resolved IAW features are measured with a 750 mm spectrometer and a streak camera, and the spectral resolution is 0.057 nm in FWHM.

In the simulations, the octahedral spherical hohlraum with six LEHs is simplified as a spherical hohlraum with two LEHs, by equating the sum of the LEH areas, as can be seen in Fig. 9, where the equivalent LEH radius is 1.16 mm. Similarly, the laser arrangement is also simplified as two cones with a single incident angle relative to the hohlraum axis. Figures 9(a) and 9(b) show maps of the electron temperature at $t = 2$ ns (the heater main pulse starts at $t = 1.5$ ns) from simulations without and with the probe beam, respectively. It can be clearly seen that the electron temperature along the laser paths is higher than in the surrounding areas and that the electron temperature along the hohlraum axis in Fig. 9(b) is higher owing to heating by the probe beam.

Figure 10(a) shows the Thomson scattering spectra measured at the hohlraum center. Owing to the geometrical symmetry, the plasma flow velocity at the hohlraum center is quite small; thus, the Doppler shift of the spectra is small and the IAW features barely twist as in the previous results shown in Fig. 5. The simulated spectra without and with the probe beam are shown in Figs. 10(b) and 10(c), respectively. Despite the differences in detail, there is a similar pattern of evolution among Figs. 10(a)–10(c). The evolution can be divided roughly into three stages: the first stage is before 2.8 ns, where the IAW features have a small separation; the second stage is from 2.8 ns to 4 ns, where the signal weakens and the IAW separation increases; and the third stage is after 4 ns, where the signal strengthens again. This pattern of evolution also appears in Fig. 11, where the evolution of the electron temperature T_e and that of the ion temperature T_i are compared between experiment and simulation. In the first stage, both T_e and T_i are quite low, and the heating effect of the probe beam is noticeable; in the second stage, both T_e and T_i increase, while T_e grows faster than T_i,
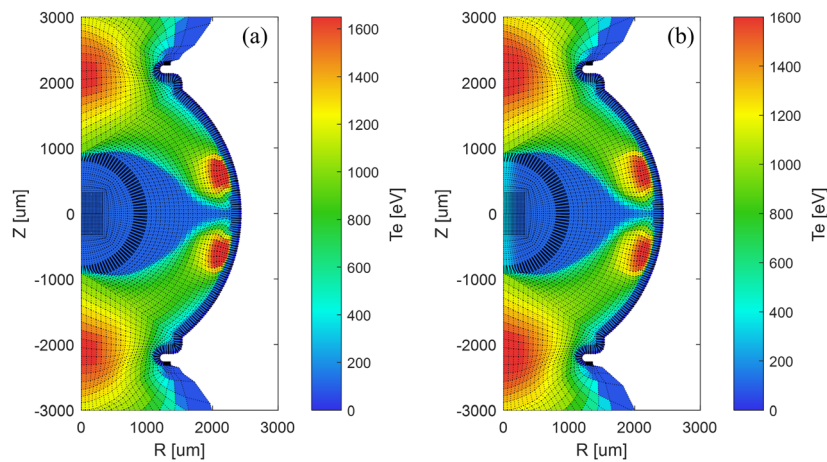

FIG. 9. Spherical hohlraum simulation maps for the electron temperature T_e at $t = 2$ ns. (a) Simulation without probe beam. (b) Simulation with probe beam. Note that the electron temperature along the Z axis is higher in (b).
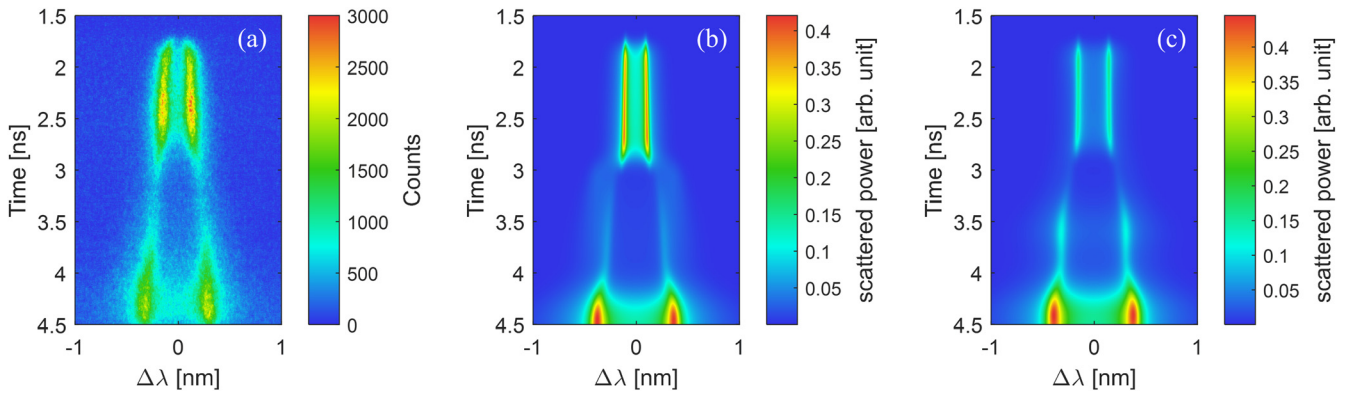
FIG. 10. Comparison of experimental and simulated Thomson scattering spectra for octahedral spherical hohlraum (diagnosed at hohlraum center). (a) Measured spectra in experiment. (b) Simulated spectra without probe beam. (c) Simulated spectra with probe beam.

which is mainly caused by electron thermal conduction; in the third stage, T_e increases slowly while T_i increases sharply, which is due to convergence of shock waves in the hohlraum. A major discrepancy between simulation and experiment is the increase in T_e after 2.8 ns, as shown in Fig. 11(a). The simulation uses the classical Spitzer–Härm model for electron thermal conduction, which accounts for local effects and gives a sharp increase in T_e. However, the experimental result shows a much slower increase in T_e, which indicates the occurrence of nonlocal electron thermal conduction[28,29] in the hohlraum.

V. SUMMARY

OTS diagnostics have been continuously developed on a series of large laser facilities for ICF research in China. Recent progress in characterizing gas-filled hohlraum plasmas has been briefly reviewed here. In the analysis of plasma evolution, two methods have been combined: spectral fitting based on experiment and spectral synthesis based on radiation-hydrodynamic simulation. By synthesizing time-resolved Thomson scattering spectra based on the LARED code, we have built up a predictive capability that can contribute to

experimental design and to understanding plasma behavior. An experiment with a simplified cylindrical hohlraum has been conducted on a 10 kJ-level laser facility, where the geometry is designed to be quasi-2D to allow comparison with 2D simulations. The plasma evolution around the LEH has been discussed, and the dynamic effects of the blast wave from the covering membrane and the convergence of shocks on the hohlraum axis have been observed. The electron temperature, ion temperature, and plasma flow velocity inferred from the measured spectra are in accordance with the simulation results, except for some differences in detail, which are due to asymmetries in the experiment. Another experiment with an octahedral spherical hohlraum has been conducted on a 100 kJ-level laser facility, and the plasma evolution at the hohlraum center has been discussed. The evolution of the electron and ion temperatures exhibits a three-stage pattern, with the heating effect of the probe beam being noticeable in the first stage, when the plasma temperature is relatively low. A major discrepancy appears as the electron temperature rises, which indicates nonlocal effects of the heat flux and requires further investigation. These preliminary studies with OTS diagnostics have established its capability to measure plasma conditions inside a hohlraum and to enable studies of detailed physical processes during plasma evolution,
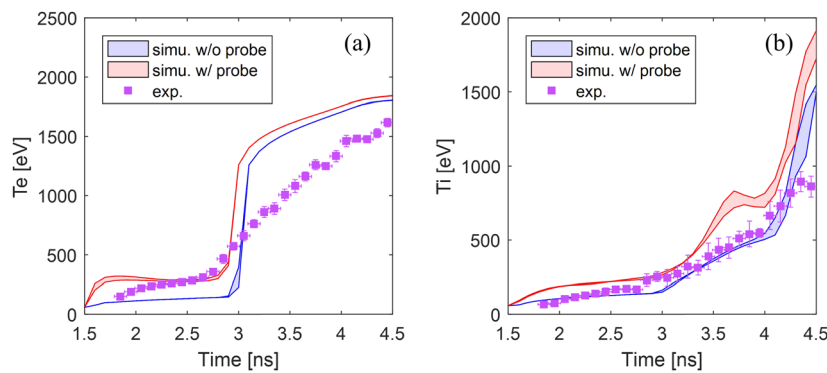

FIG. 11. Evolution of plasma parameters at the hohlraum center ($Z = 0$, $R = 0$ in the simulations). (a) Electron temperature. (b) Ion temperature. The squares are inferred from experimental data. The red and blue lines are from simulations with and without the probe beam, respectively, and the shaded areas characterize the plasma inhomogeneity within the Thomson scattering volume.

which will be of great importance in gaining a better understanding of laser–hohlraum coupling.

REFERENCES

[1]J. D. Lindl, P. Amendt, R. L. Berger, S. G. Glendinning, S. H. Glenzer et al., "The physics basis for ignition using indirect-drive targets on the National Ignition Facility," Phys. Plasmas **11**, 339 (2004).

[2]W. L. Kruer, *The Physics of Laser Plasma Interactions* (Addison-Wesley Publishing Company, 1988).

[3]J. Lindl, O. Landen, J. Edwards, E. Moses, and NIC Team, "Review of the National Ignition Campaign 2009–2012," Phys. Plasmas **21**, 020501 (2014).

[4]N. B. Meezan, M. J. Edwards, O. A. Hurricane, P. K. Patel, D. A. Callahan et al., "Indirect drive ignition at the National Ignition Facility," Plasma Phys. Control. Fusion **59**, 014021 (2017).

[5]D. H. Froula, S. H. Glenzer, N. C. Luhmann, and J. Sheffield, *Plasma Scattering of Electromagnetic Radiation: Theory and Measurement Techniques* (Academic Press, 2011).

[6]D. H. Froula, J. S. Ross, L. Divol, and S. H. Glenzer, "Thomson-scattering techniques to diagnose local electron and ion temperatures, density, and plasma wave amplitudes in laser produced plasmas," Rev. Sci. Instrum. **77**, 10E522 (2006).

[7]R. K. Follett, J. A. Delettrez, D. H. Edgell, R. J. Henchen, J. Katz et al., "Plasma characterization using ultraviolet Thomson scattering from ion-acoustic and electron plasma waves," Rev. Sci. Instrum. **87**, 11E401 (2016).

[8]S. H. Glenzer, W. Rozmus, B. J. MacGowan, K. G. Estabrook, J. D. De Groot et al., "Thomson scattering from high-Z laser-produced plasmas," Phys. Rev. Lett. **82**, 97 (1999).

[9]J. S. Ross, H. S. Park, P. Amendt, L. Divol, N. L. Kugland et al., "Thomson scattering diagnostic for the measurement of ion species fraction," Rev. Sci. Instrum. **83**, 10E323 (2012).

[10]S. H. Glenzer, C. A. Back, L. J. Suter, M. A. Blain, O. L. Landen et al., "Thomson scattering from inertial-confinement-fusion hohlraum plasmas," Phys. Rev. Lett. **79**, 1277 (1997).

[11]S. H. Glenzer, T. L. Weiland, J. Bower, A. J. MacKinnon, and B. J. MacGowan, "High energy 4ω probe laser for laser-plasma experiments at Nova," Rev. Sci. Instrum. **70**, 1089 (1999).

[12]D. H. Froula, J. S. Ross, L. Divol, N. Meezan, A. J. Mackinnon et al., "Thomson-scattering measurements of high electron temperature hohlraum plasmas for laser-plasma interaction studies," Phys. Plasmas **13**, 052704 (2006).

[13]J. S. Ross, "Measurements of relativistic effects in collective Thomson scattering at electron temperatures less than 1 keV," Ph.D. thesis, University of California, San Diego, 2010.

[14]J. S. Ross, D. H. Froula, A. J. Mackinnon, C. Sorce, N. Meezan et al., "Implementation of imaging Thomson scattering on the Omega laser," Rev. Sci. Instrum. **77**, 10E520 (2006).

[15]J. S. Ross, P. Datte, L. Divol, J. Galbraith, D. H. Froula et al., "Simulated performance of the optical Thomson scattering diagnostic designed for the National Ignition Facility," Rev. Sci. Instrum. **87**, 11E510 (2016).

[16]B. Bai, J. Zheng, W. Liu, C. X. Yu, X. Jiang et al., "Thomson scattering measurement of gold plasmas produced with 0.351 μm laser light," Phys. Plasmas **8**, 4144 (2001).

[17]Z. Wang, J. Zheng, B. Zhao, C. X. Yu, X. Jiang et al., "Thomson scattering from laser-produced gold plasmas in radiation conversion layer," Phys. Plasmas **12**, 082703 (2005).

[18]Z. Li, J. Zheng, X. Jiang, Z. Wang, D. Yang et al., "Interaction of 0.53 μm laser pulse with millimeter-scale plasmas generated by gasbag target," Phys. Plasmas **19**, 062703 (2012).

[19]T. Gong, Z. Li, X. Jiang, Y. Ding, D. Yang et al., Rev. Sci. Instrum. **86**, 023501 (2015).

[20]H. Zhao, Z. Li, D. Yang, X. Jiang, Y. Liu et al., Rev. Sci. Instrum. **89**, 093505 (2018).

[21]W. Pei, "The construction of simulation algorithms for laser fusion," Commun. Comput. Phys. **2**, 255 (2007).

[22]K. Lan, J. Liu, Z. Li, X. Xie, W. Huo et al., "Progress in octahedral spherical hohlraum study," Matter Radiat. Extremes **1**, 8 (2016).

[23]J. Zheng, C. X. Yu, and Z. J. Zheng, "The dynamic form factor for ion-collisional plasmas," Phys. Plasmas **6**, 435 (1999).

[24]J. Zheng, C. X. Yu, and Z. J. Zheng, "Effects of non-Maxwellian (super-Gaussian) electron velocity distribution on the spectrum of Thomson scattering," Phys. Plasmas **4**, 2736 (1997).

[25]J. Dawson and C. Oberman, "High frequency conductivity and the emission and absorption coefficients of a fully ionized plasma," Phys. Fluids **5**, 517 (1962).

[26]K. Lan and W. Zheng, "Novel spherical hohlraum with cylindrical laser entrance holes and shields," Phys. Plasmas **21**, 090704 (2014).

[27]W. Huo, Z. Li, Y. Chen, X. Xie, G. Ren et al., Phys. Rev. Lett. **120**, 165001 (2018).

[28]S. H. Glenzer, W. E. Alley, K. G. Estabrook, J. S. De Groot, M. G. Haines et al., "Thomson scattering from laser plasmas," Phys. Plasmas **6**, 2117 (1999).

[29]G. Gregori, S. H. Glenzer, J. Knight, C. Niemann, D. Price et al., "Effect of nonlocal transport on heat-wave propagation," Phys. Rev. Lett. **92**, 205006 (2004).